PERGAMON

International Journal of Heat and Mass Transfer 43 (2000) 85–99

International Journal of HEAT and MASS TRANSFER

www.elsevier.com/locate/ijhmt

Evaporative heat transfer from thin liquid film on a heated cylinder

J. Jiang[a], Y.-X. Tao[a,*], L. Byrd[b]

[a]*Department of Mechanical Engineering, Tennessee State University, Nashville, TN 37209-1561, USA*
[b]*Structure Dynamics Division, Air Force Research Laboratory, Wright Patterson AFB, OH, USA*

Received 11 September 1998; received in revised form 26 March 1999

Abstract

Simulating a porous surface that is partially saturated with a liquid, a two-dimensional meniscus attaching two adjacent cylinders with the same diameter is studied under heating and convective conditions. A thin liquid film model is presented to predict thin film thickness and evaporative heat transfer coefficient. Experiments are carried out to characterize the temperature and geometry of a liquid meniscus. The evaporating thin film length is determined from measured surface temperature and meniscus shape. The surface temperature data is correlated and used to derive the evaporative heat transfer coefficient with the aid of conjugate heat transfer using a finite element code. The results are compared reasonably with the thin film model. The effects of Bond number, spacing between cylinders and heating power on thin film geometry and heat transfer characteristics are discussed. Correlations to predict the evaporative heat transfer coefficient and ratio of evaporative heat transfer rate to total heat rate are presented.

1. Introduction

High heat transfer rate from liquid thin film is believed to be responsible for the maximum heat transfer during boiling and the wetting characteristics in porous media during dryout. General applications include the cooling of gas turbine blades, nuclear fuel elements in a hypothetical accident, and the first wall and diverter-plate of fusion reactors. Conceptual application of the electrostatic liquid film radiator to space power cycles was also proposed [1]. The idea is to attain very high heat fluxes by stabilizing the liquid film, which is not an easy task. Many unanswered questions remain before any engineering applications of such sustainable thin film concept are practical. Here, the thin film is defined as having a typical thickness of the order of a few micrometers. The basic research in thin film phase change heat transfer can be categorized by three groups: equilibrium thin films with static contours, phase change thin films (evaporation and condensation, temperature gradients, dynamic contours, and instability), and multiple physical effects (thin film flow and heat transfer, multi-components liquid, or in the electrostatic field).

The static equilibrium of a liquid surface in contact with a solid is traditionally described by the classic Young–Laplace equation which is based on static, or macroscopic, force balance without considering the intermolecular forces near the liquid–solid–fluid inter-

* corresponding author. Tel.: +1-615-963-5390; fax: +1-615-963-5496.
E-mail address: taoy@harpo.tnstate.edu (Y.X. Tao)

0017-9310/00/$ - see front matter
PII: S0017-9310(99)00117-9

Nomenclature

B	coefficient in Eq. (9), Pa m^3
Bo	Bond number, $g\rho_l R_{cyl}^2/\sigma$
g	gravitational acceleration, m/s^2
h	heat transfer coefficient, W/m^2 K
H	curvature, 1/m
k	thermal conductivity, W/m K
l_d	characteristic length of the evaporating film transition region
q	heating power per unit length, W/m
q''	heat flux, W/m^2
R	radius, m
S	arc length, m
T	temperature, °C
x	coordinate, m
X	distance between the center of cylinder and contact line, m
y	coordinate, m.

Greek symbols

δ	thin film thickness, m
η	coordinate, m
μ	viscosity, Pa s
ξ	coordinate, m
ρ	density, kg/m^3
σ	surface tension, N/m.

Subscripts

cyl	cylinder
eva	evaporation
f	thin film
l	liquid
s	static; solid surface
sl	solid–liquid interface
sph	equivalent sphere
w	at contact point of the static contour
0	at $x = 0$ or $\xi = 0$.

Other

$\bar{}$	(over) dimensionless
$\langle\ \rangle$	average.

faces in the so-called thin film region [2]:

$$p_g - p_l = 2\sigma H, \tag{1}$$

where H is the average, or local, curvature of the gas–liquid interface which is defined by an intrinsic contact angle through the Young's equation [3]. The intrinsic contact angle can be determined if the solid surface is perfectly clean and smooth. In engineering applications, this condition is rarely met. Also, a reliable measurement technique for the contact angle has to be developed. Therefore, application of the Young–Laplace equation to many practical problems is still questionable. It has been generally agreed, however, that away from the contact line of the liquid–fluid–solid interface, the Young–Laplace equation predicts the contour of the liquid–fluid interface reasonably well. This observation lays a foundation for determining the saturation of liquid in a porous media from a particle-scale model [2].

To consider the intermolecular surface effects in the thin film region near the liquid–solid–fluid interfaces, two approaches have been used [4]. One is to allow the surface tension varying with the physical location of the thin film, and the other is to introduce the disjoining pressure concept to modify the pressure term in the Young–Laplace equation, referred to as the modified Young–Laplace equation as follows.

$$p_g - p_l = 2\sigma H + p_d, \tag{2}$$

where p_d is the disjoining pressure. Both approaches reflect the same physical phenomena of intermolecular interaction among the phases involved within the thin liquid film region. Direct experimental confirmation of these models is currently lacking. In the absence of better models and experimental data, the modified Young–Laplace model is still widely used, even in the cases where the phase interfaces are subject to non-isothermal boundary conditions. The model provides the very basic description of the liquid–solid–fluid interface shape, thin film thickness and length, and thin film heat transfer area. These results are essential to estimate the surface heat transfer coefficient. It has been categorized that the thin film is composed of an evaporating thin film part and a non-evaporating, extended thin film part that is in equilibrium with the exposed solid phase and of the order of nanometers. Several studies have been devoted to the development of the model which is demonstrated for a thin film attaching a flat surface [4,5].

Since thin film heat transfer has a potential to enhance the local heat transfer rate, studies have been carried out to investigate the mechanisms that stabilize or destabilize the thin film over a solid surface. Bankoff [1] summarized a series of studies carried out by his team. The focuses of their studies are the nonlinear stability of an evaporating one-component liquid film, long-wave instabilities of heated falling films and local dry-out of a horizontal heated film. The essential

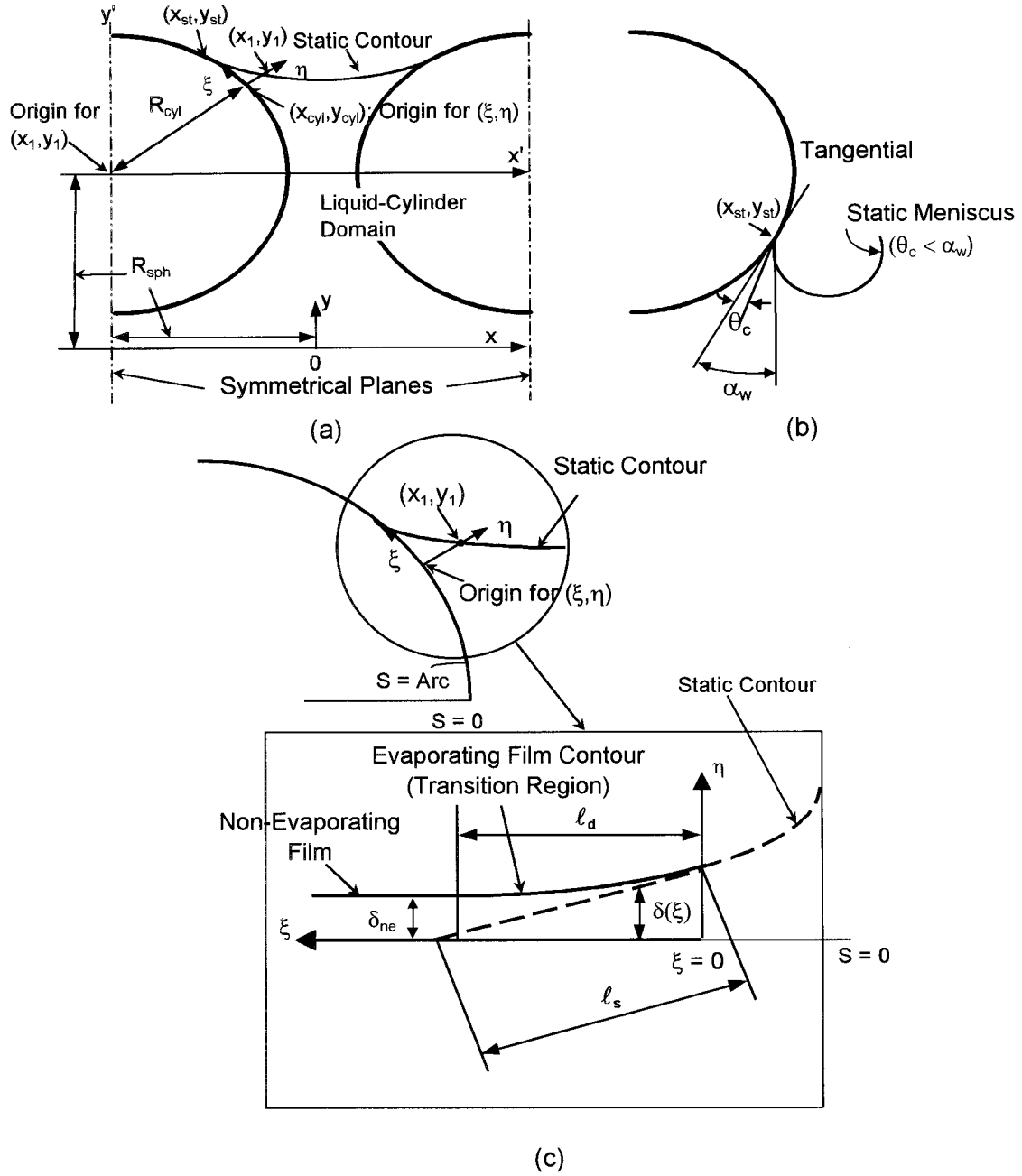

Fig. 1. Model of liquid-curved solid–fluid contact region: (a) computational domains; (b) definition of α_w for the static contour in contact with the lower part of the fiber; and (c) definition of the transition region for evaporating film.

approach in instability studies is to analyze the response of a thin film that is subject to an initial perturbation, a given surface contour. Williams and Davis [6] included van der Waals attraction and surface tension effects. Burelbach et al. [7] later extended the work to include thermal capillary, evaporative and non-equilibrium vaporization effects. Joo et al [8] further included falling films on an inclined plate to arrive at a generalized formula that is applied to both two- and three-dimensional surface instabilities.

To better understand the characteristics of evaporative heat transfer near thin film region and validate

important parameters in model prediction, experimental confirmation is necessary. Burelbach et al. [7] performed experiments of thin film thickness and temperature for an initially 0.38 mm thick, silicone oil layer. The data show a measured minimum thickness of about 0.13 mm which may not be representative for thinner films. DasGupta et al. [9] used an imaging analysis method to measure the evaporating thin film near the interfacial contact line on a flat surface. Tao and Kaviany [10] reported that the measured meniscus–solid interface line deviates significantly from the prediction based on the Young–Laplace equation, suggesting that a significant portion of the surface beyond that described by the Young–Laplace static model could be the thin-film region. If this correction is made, the resulting temperature profile matches much better to the experimental data obtained from the high resolution infrared imager. So far, no data of evaporating thin film near the interfacial contact line are available for curved surfaces such as cylinders.

Motivated by the above observation, we focus on development of a prediction method for heat transfer characteristics in the thin film region using a two-dimensional physical model. The objective is to construct a representative model that includes such effects as combined liquid motion, and heat transfer (with and without phase change) near the fluid–liquid–solid contact line. We select a simple model for fluid interaction with non-flat solid surfaces: a cylindrical fiber model. This attempt allows the simulation of a porous surface that is partially saturated with a liquid [10], and could be scaled down for studying the effect of surface roughness. The model considers adjacent cylinders with the same diameters and under heating and convective conditions. In this paper the following specific approaches are taken:

1. Experiments are conducted for different heating conditions of partially liquid covered cylinders to quantify the characteristic evaporating length (equivalent to evaporating surface area per unit cylinder length) and surface temperature of both liquid and solid.
2. A numerical model using the disjoining pressure concept (thin film model) is developed to determine the thin film geometry, liquid velocity within the thin film and heat transfer coefficient.
3. Convective heat transfer within the liquid is simulated using a finite element code with the specified surface temperature obtained from experiments. From this conjugate heat transfer model combined with experimental results, the semi-empirical, surface evaporative heat transfer coefficient and heat transfer rate of evaporating thin film are obtained. The results are to be compared with that of the thin film model.

2. Theoretical background

A unit cell of two-dimensional meniscus attaching two adjacent cylinders with the same diameters is defined subject to heating in the solid and convection in the gas phase. Formulation is divided into three components: static meniscus contour, transition region meniscus contour (the thin film model), and heat transfer and flow model (the finite element model). The transition region includes the connection between bulk meniscus and the thin film region which contains evaporating and non-evaporating thin films.

Fig. 1 shows the definitions of these computational domains. The x–y coordinate system is for the static meniscus contour with the origin in the center bottom of the liquid region. The thin film region is described by the ξ–η coordinate system with the origin at the solid–liquid interface away from the contact line. The static contact line is defined by (x_{st}, y_{st}). R_{sph} denotes one-half of the distance between the centers of two adjacent cylinders, and can be treated as the radius of hypothetical equivalent spheres that have the same centers as cylinders and are in parallel contact. Other symbols of the variables and parameters are listed in the Nomenclature or explained in the following sections. In this paper, a quantity with a bar over it indicates that the quantity is dimensionless.

2.1. Meniscus contour model

2.1.1. Static meniscus

Depending on the contact line location on the cylinder and apparent (intrinsic), static contact angle, θ_c, the static contour can be derived from the Young–Laplace Eq. (1) and described by the following dimensionless forms [2,9]:

1. $\theta_c > \alpha_w$:

$$\frac{d^2\bar{y}}{d\bar{x}^2} = -(\bar{p}_{l0} - Bo\,\bar{R}^{-2}\bar{y})\left[1 + \left(\frac{d\bar{y}}{d\bar{x}}\right)^2\right]^{1.5}, \tag{3}$$

where

$$\bar{x} = \frac{x}{R_{sph}}, \quad \bar{y} = \frac{y}{R_{sph}}, \quad \bar{p}_{l0} = \frac{p_{l0}R_{sph}}{\sigma},$$

$$Bo = \frac{g\rho_l R_{cyl}^2}{\sigma}, \quad \bar{R} = \frac{R_{cyl}}{R_{sph}},$$

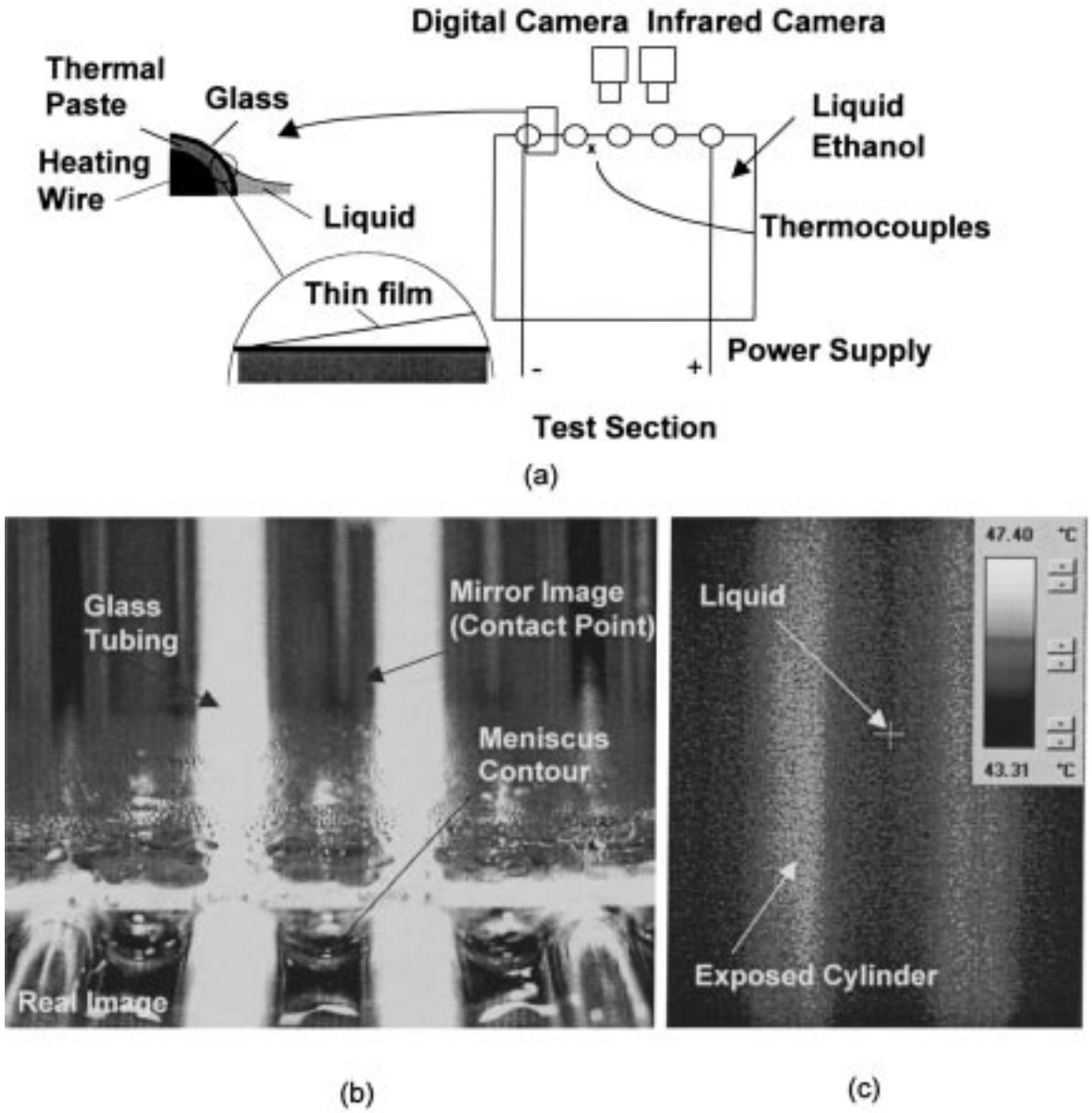

Fig. 2. Experiment: (a) test equipment; (b) photograph of the liquid meniscus in contact with heated cylinders; and (c) infrared image of liquid–solid surface.

and the characteristic angle α_w is depicted in Fig. 1(b).

2. $\theta_c < \alpha_w$:

$$\frac{d^2\bar{x}}{d\bar{y}^2} = -(\bar{p}_{l0} - Bo\,\bar{R}^{-2}\bar{y})\left[1 + \left(\frac{d\bar{x}}{d\bar{y}}\right)^2\right]^{1.5}, \quad \text{for } x \le -|x_{st}|, \tag{4}$$

$$\frac{d^2\bar{y}}{d\bar{x}^2} = -(\bar{p}_{l0} - Bo\,\bar{R}^{-2}\bar{y})\left[1 + \left(\frac{d\bar{y}}{d\bar{x}}\right)^2\right]^{1.5}, \quad \text{for } -|x_{st}| < x < |x_{st}|, \tag{5}$$

$$\frac{d^2\bar{x}}{d\bar{y}^2} = (\bar{p}_{l0} - Bo\,\bar{R}^{-2}\bar{y})\left[1 + \left(\frac{d\bar{x}}{d\bar{y}}\right)^2\right]^{1.5}, \quad \text{for } x \ge |x_{st}|. \tag{6}$$

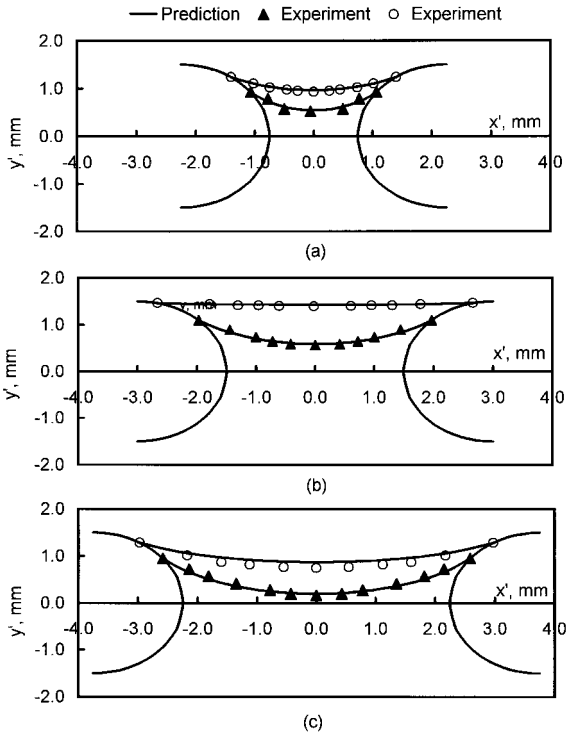

Fig. 3. The static meniscus contour (liquid: ethanol).

The boundary conditions for the above equations are:

$$\frac{d\bar{y}}{d\bar{x}}(0) = 0, \tag{7}$$

$$\bar{y}_{st} = \pm\sqrt{\bar{R}^2 - (1+\bar{x}_{st})^2}. \tag{8}$$

2.1.2. Transition region

Fig. 1(c) shows the definitions of the specified transition region length, l_s, based on the static meniscus contour, and the calculated characteristic length of transition region, l_d. The arc length of the cylinder, S, with the origin defined in Fig. 1(a) is to be used to show the results of l_d in the discussion section. δ and δ_{ne} are the evaporating and non-evaporating film thickness, respectively. After derivation, the modified Young–Laplace Eq. (2) yields the following:

$$\frac{d^2\bar{\delta}}{d\bar{\xi}^2} = \frac{\dfrac{\bar{B}}{\bar{\delta}^3} - (\bar{p}_{l,0} + Bo\,\bar{y}_{\xi}\bar{R}^{-2})}{\left[1+\left(\dfrac{d\bar{\delta}}{d\bar{\xi}}\right)^2\right]^{1.5}}, \tag{9}$$

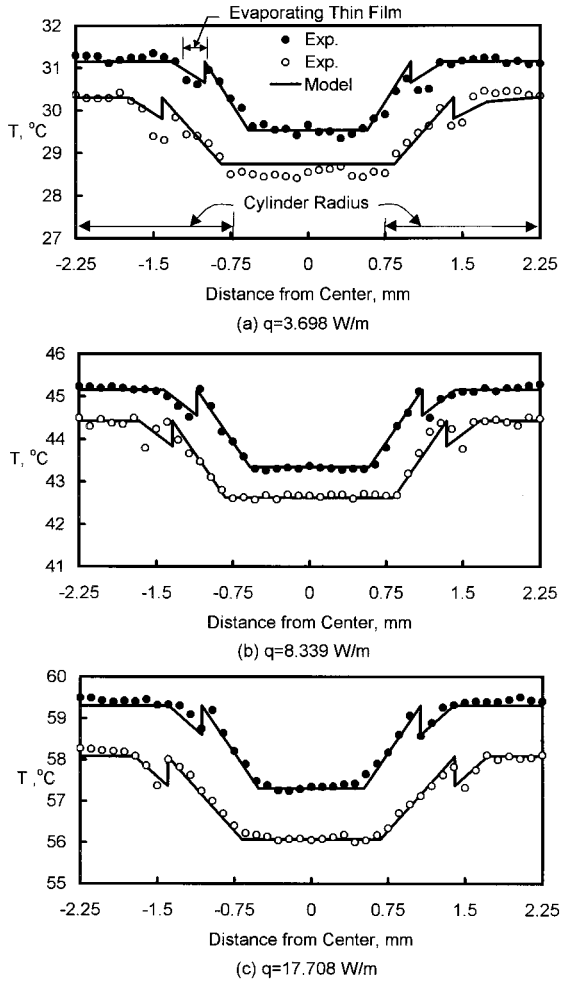

Fig. 4. Measured surface temperature of liquid and exposed glass cylinder at different power supplied (R_{sph} = 2.25 mm).

where

$$\bar{B} = \frac{B}{\sigma R_{sph}^2}, \quad \bar{\delta} = \frac{\delta}{R_{sph}}, \quad \bar{\xi} = \frac{\xi}{R_{sph}}.$$

The boundary conditions for the transition region are:

$$\bar{\delta}(\bar{\xi}=0) = \sqrt{(\bar{x}_1 - \bar{x}_{cyl})^2 + (\bar{y}_1 - \bar{y}_{cyl})^2}, \tag{10}$$

$$\frac{d^2\bar{\delta}}{d\bar{\xi}^2}(\bar{\xi}\to\bar{l}_d) = 0, \tag{11}$$

where

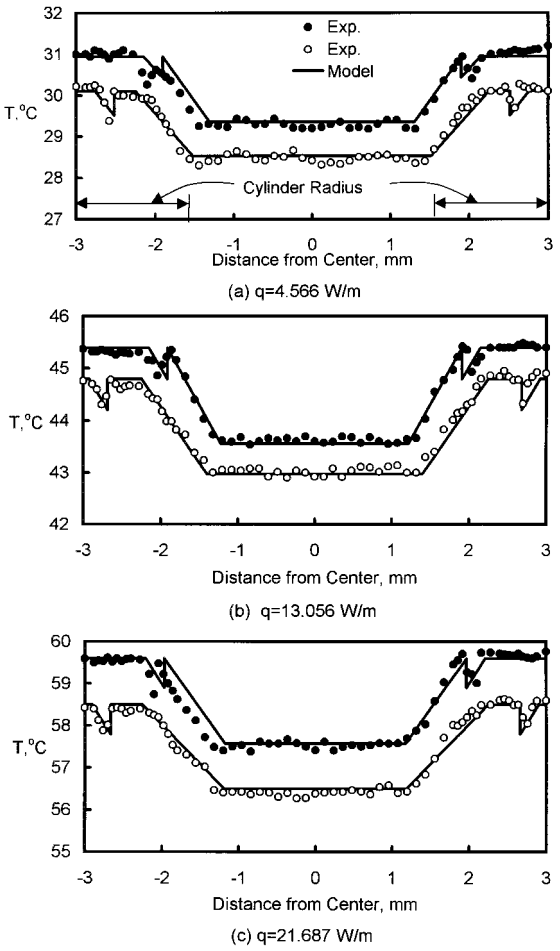

Fig. 5. Measured surface temperature of liquid and exposed glass cylinder at different power supplied ($R_{sph}=3.00$ mm).

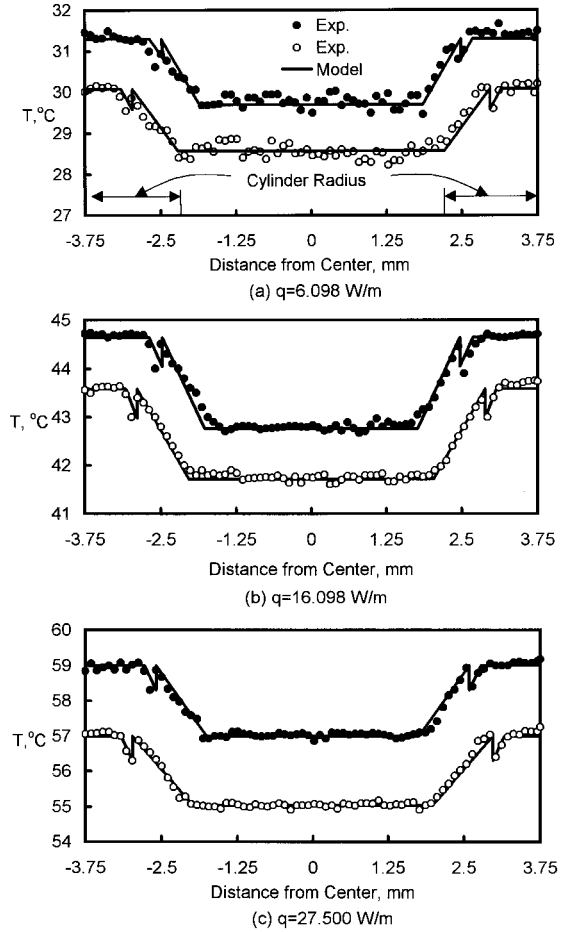

Fig. 6. Measured surface temperature of liquid and exposed glass cylinder at different power supplied ($R_{sph}=3.75$ mm).

$$\bar{x}_{cyl} = -1 \pm \frac{\bar{R}}{\sqrt{\frac{\bar{y}_1^2}{(1+\bar{x}_1)^2}+1}}, \quad \bar{y}_{cyl} = \sqrt{\bar{R}^2 - \bar{x}_{cyl}^2},$$

$$\bar{l}_d = \frac{l_d}{R_{sph}}.$$

Eq. (11) indicates the condition at the starting location of the non-evaporating film as depicted in Fig. 1(c). Another boundary condition is:

$$\frac{d\bar{\delta}}{d\bar{\xi}}(\bar{\xi}=0) = \frac{-\bar{y}_1 \sin\alpha - \cos\alpha}{\sin\alpha - \bar{y}_1 \cos\alpha}, \tag{12}$$

where $\bar{x}_1$ ($=x_1/R_{sph}$) and $\bar{y}_1$ ($=y_1/R_{sph}$) are defined in the x'–y' coordinate system and obtained from the solution of the static meniscus contour at the location where the characteristic length of the transition region, l_s, is defined (see Figs. 1(a) and (c)). We also have the following geometric constraint that is incorporated into Eq. (9)

$$\bar{y}_\xi = (R+\bar{\delta})\sin\alpha + 1, \tag{13}$$

where

$$\alpha = \tan^{-1}\frac{\bar{y}_1}{\bar{x}_1} + \frac{\Delta\bar{\xi}}{\bar{R}},$$

and the following coordinate transformation between $(\bar{x}, \bar{y})$ and $(\bar{x}_1, \bar{y}_2)$ (see Figs. 1(a) and (c)) is used:

$$\bar{x}_1 = 1 + \bar{x}, \quad \bar{y}_1 = \bar{y} - 1.$$

2.1.3. Average velocity of the evaporating film

According to the coordinates shown in Fig. 1(c), we used the same momentum formulation (lubrication theory) as outlined by Wayner [11]:

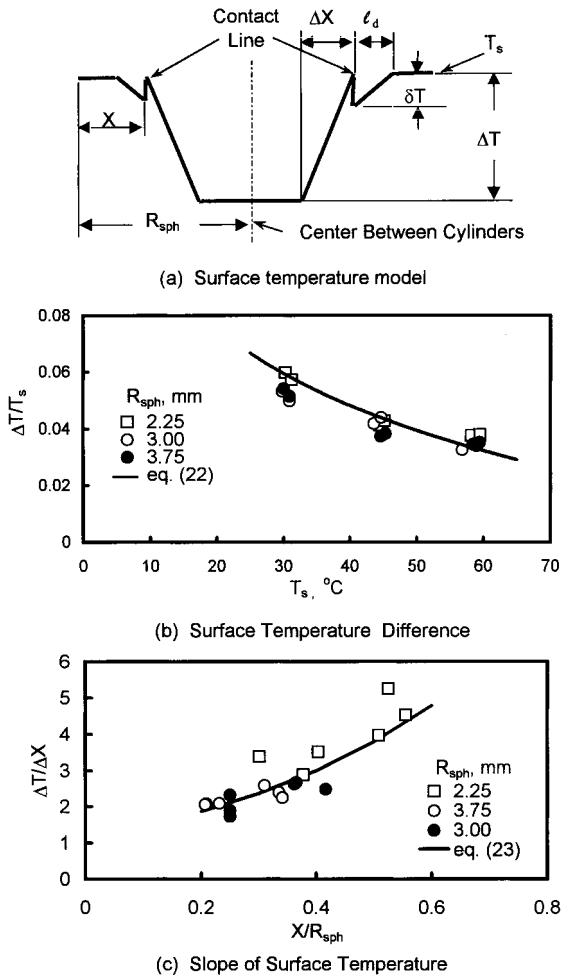

Fig. 7. Surface temperature distribution: (a) model; (b) temperature difference; and (c) slope.

$$\frac{d^2\bar{v}_l}{d\bar{\eta}^2} = 3\frac{\bar{B}}{\bar{\delta}^4}\frac{d\bar{\delta}}{d\bar{\xi}}, \tag{14}$$

where the dimensionless liquid velocity and vertical coordinate in the thin film region are defined, respectively, as

$$\bar{v}_l = \frac{\bar{v}_l\mu_l}{\sigma}, \quad \bar{\eta} = \frac{\eta}{R_{sph}}.$$

To consider the effect of shear stress the external flow may exert on the transition meniscus, the following boundary conditions include the interfacial shear stress term, τ_{lg}:

$$\bar{v}_l(\bar{\eta} = 0) = 0, \tag{15}$$

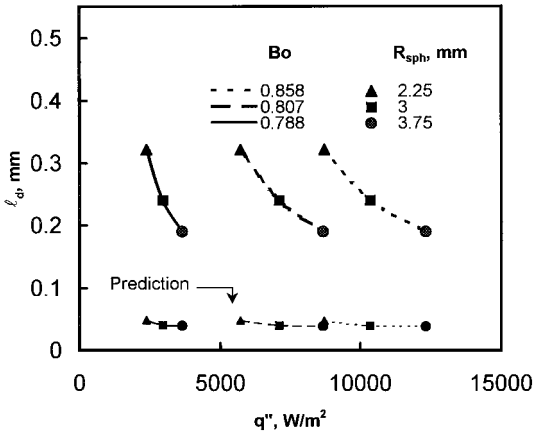

Fig. 8. Evaporating thin film length.

$$\frac{d\bar{v}_l}{d\bar{\eta}}(\bar{\eta} = \bar{\delta}) = \tau_{lg}, \tag{16}$$

where

$$\bar{\tau}_{lg} = \frac{\tau_{lg}R_{sph}}{\sigma}.$$

Integration of Eq. (14) over $0 \le \bar{\eta} \le \bar{\delta}$ yields

$$\langle\bar{v}_l\rangle = \frac{\bar{\tau}_{lg}\,\bar{\delta}}{2} + \frac{\bar{B}}{\bar{\delta}_l^2}\frac{d\bar{\delta}}{d\bar{\xi}}, \tag{17}$$

where the symbol $\langle\ \rangle$ implies that the velocity is averaged over $\bar{\delta}$.

2.1.4. Surface energy balance

Assuming conduction heat transfer is balanced by energy of vaporization, we have the following dimensional equation:

$$\frac{k_l}{\delta}(T_{lg} - T_{sl})\Delta\xi = \rho_l\langle v_l\rangle\Delta h_{fg}. \tag{18}$$

The dimensionless temperature of the thin film surface can be determined from the following equation:

$$\bar{T}_{lg} = \bar{T}_{sl} - Ja\,Pe\frac{\Delta\bar{\delta}}{\Delta\bar{\xi}}, \tag{19}$$

where the Peclet number $Pe = \langle v_l\rangle\delta/\alpha_l$, the Jacob number $Ja = h_{fg}/(c_p\Delta T)$, and $\bar{T} = T/\Delta T$. The local heat transfer coefficient can be found from the following definition:

$$h = \frac{k_l(T_{lg} - T_{sl})/\delta}{\Delta T}. \tag{20}$$

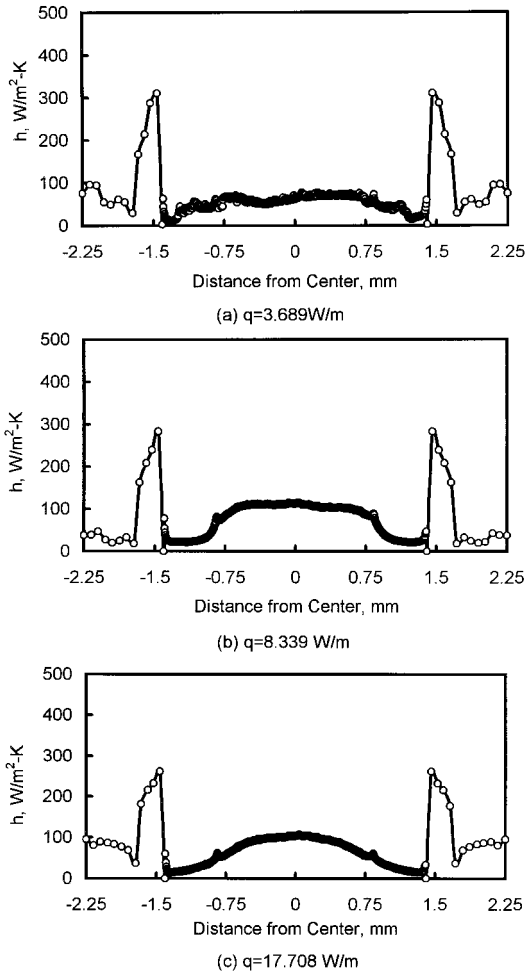

Fig. 9. Surface heat transfer coefficient distribution ($R_{sph}=2.25$ mm).

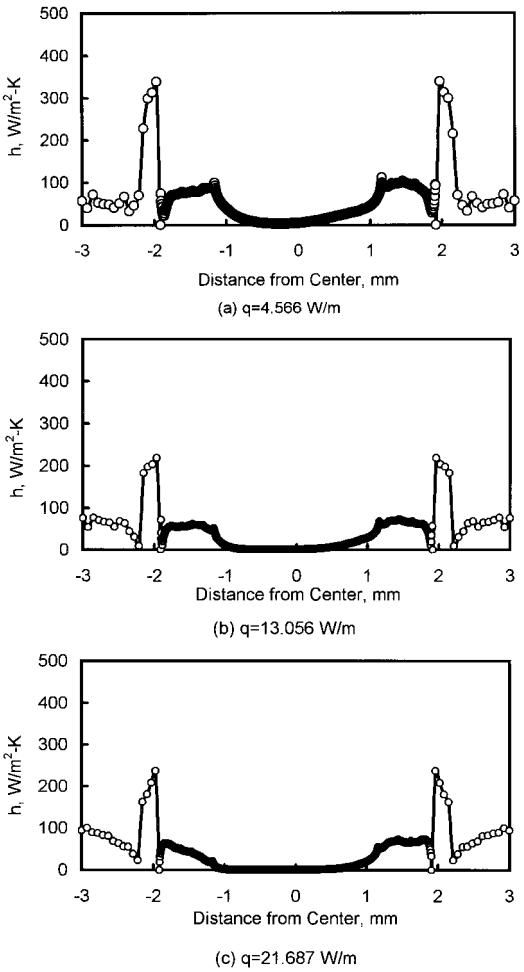

Fig. 10. Surface heat transfer coefficient distribution ($R_{sph}=3.00$ mm).

2.2. Flow and heat transfer modeling

The conduction in the cylinder and convection in the liquid are analyzed using a commercial CFD finite element code, COSMOS/M with the FLOWPLUS option. The following assumptions are made:

1. Natural convection occurs in the liquid.
2. Uniform energy generation is considered for the heating element part of the composite cylinder. The outer shell of the cylinder is glass, and conducting paste is sandwiched between the glass and the heating material.
3. Constant thermophysical properties are assumed except for the liquid density which varies with temperature.
4. Evaporation from the transition region of the meniscus is accounted for by specifying the top surface temperature obtained from experiments.
5. Shear stress on the meniscus is nearly zero such that no physical instability of liquid surface due to perturbation is considered.
6. The non-evaporating thin film thickness is very thin. Only static meniscus geometry is used in generating the mesh for liquid.

The mathematical formulation for the above-defined convection problem is standard. The adiabatic boundary conditions are imposed on the symmetric planes of the computational domain and on the bottom of the liquid domain (see Fig. 1(a)). The surface temperature distribution on the liquid meniscus and the exposed solid, $\bar{T}_{sl}$, is specified from a correlation model developed from the experimental results, as will be discussed in the Section 4.2. This semi-empirical treatment allows the relatively reliable determination of heat transfer coefficient distribution over the liquid surface.

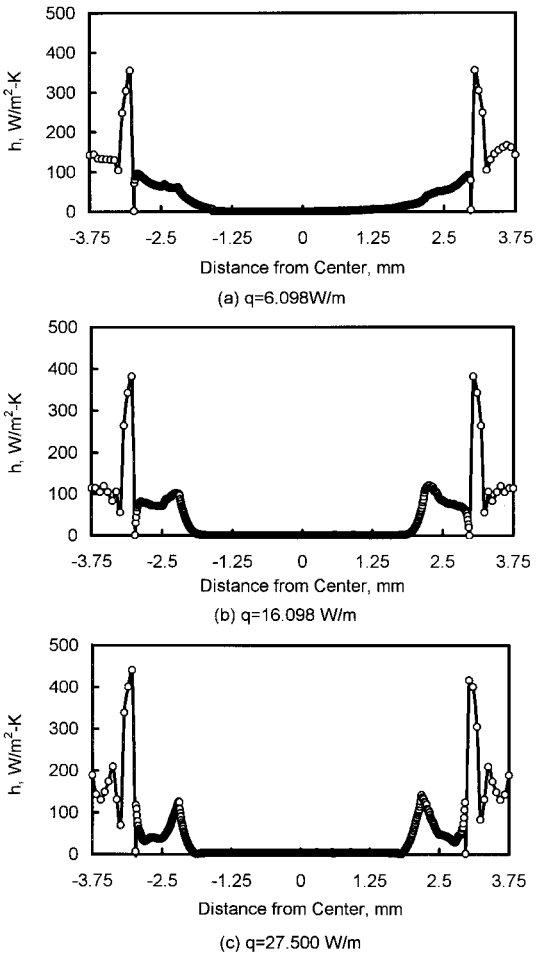

Fig. 11. Surface heat transfer coefficient distribution ($R_{sph}=3.75$ mm).

2.3. Solution method

The Runge–Kutta method is used to solve the static and transition meniscus contours with the specified $\bar{l}_s$ and $\bar{B}$. In solving the static contour, $\bar{p}_{l0}$ is initially guessed and adjusted during the iteration process until the boundary condition, Eq. (7), is satisfied [12]. For the transition region thin film contour, the advancing of the solution stops when the following condition is satisfied:

$$\frac{d\bar{\delta}}{d\bar{\xi}}(\bar{\xi}=\bar{l}_d)=0. \tag{21}$$

This equation satisfies the boundary condition (11). The shear stress at the liquid–gas interface, $\bar{\tau}_{lg}$ which is input to Eq. (14), is set zero in this study. It can be extended to other values for studying the effect of shear stress at the interface on thin film characteristics.

The false-transient method is used for the finite element, conjugate heat transfer model to find quasi-steady state temperature distribution. The normal surface temperature gradient is determined and is to be used to calculate heat transfer coefficients as will be shown in the Section 4.4. The dependence of numerical results on the mesh size is minimized by testing the results with different meshing schemes. The results are considered to reach a quasi-steady state when the total energy balance through the liquid phase is within 2%.

3. Experimental method

Fig. 2(a) shows a schematic of the test apparatus. A number of glass tubes of 3 mm outer diameter are arranged in parallel on top of a container where liquid ethanol is filled to a desired level of contact with the tube. The saturation temperature of ethanol at atmospheric pressure is 78°C. A heating wire of 1 mm diameter is inserted inside of the tube. The gap between the heating element and glass wall is filled with the thermal conducting paste to provide a good thermal contact. For a controlled power supply, different surface temperature conditions can be achieved. After carefully filling the liquid level to the predetermined level, the heater is turned on. A high resolution (1250×1500 pixels) digital camera is used to record the image of liquid meniscus contour. A mirror is mounted at the location of measurement to compensate the incident angle of camera to the imaging area. The 1250×1500 pixel digital image is then imported to computer software for image analysis. From the linear calibration of 1 mm equal to 50 pixels, the whole liquid contour and contact points with the cylinder are traced and converted to physical coordinates. The uncertainty in determining the liquid contour is estimated to be less than 1%. A quasi-steady temperature profile is achieved after about ten minutes. A FLIR system infrared camera, with a spatial resolution of 1 mm (=20 pixels), is used to obtain the thermal images of liquid and exposed solid surface. The pictures are taken by digital camera and by infrared camera at the same time. The emissivity of ethanol and glass is nearly unity, which allows relatively accurate measurement of surface temperature within a 0.1°C resolution and 2°C uncertainty. The infrared camera was calibrated by the manufacturer and also confirmed in separate tests against thermocouples readings. A set of experiments are conducted to determine the range of aiming angle for the imager such that the influence of glass surface curvature to the accuracy of infrared reading is minimized. The liquid temperatures beneath the meniscus and cylinders are measured by thermocouples within 1°C. Three spacings are chosen to study the effect of liquid convection. The contact position between the

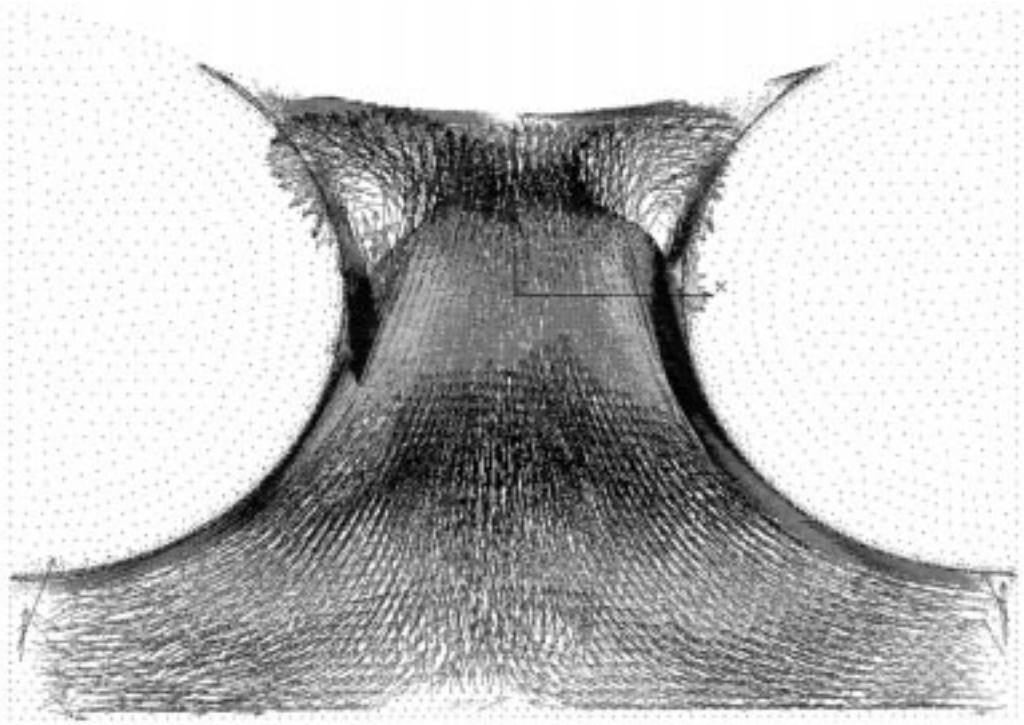

Fig. 12. Typical liquid velocity distribution.

liquid and cylinder surface is varied for different test conditions.

4. Results and discussion

4.1. Meniscus geometry

Fig. 2(b) shows the digital image of liquid meniscus contour attaching to a cylinder. We consider the visual observation of the contact point (line) is the one defined by the static Young–Laplace equation. The assumption is that the extended thin film has a thickness that cannot be resolved from the optical images with the resolution of 20 μm. From the infrared image of the liquid–surface, we map the temperature in conjunction with the optical image. An attempt is made to see whether at the location near the bulk contact line, a temperature fluctuation (decrease) can be detected as a result of evaporation and high heat transfer rate. A typical infrared image is shown in Fig. 2(c).

Fig. 3 shows the measured liquid surface contour compared well with the predicted static contour for different heating power supplies and at different liquid coverage on the cylinders. The liquid–gas–solid contact line determined in this way lays a foundation as a transitional line for thin film geometry calculation.

4.2. Surface temperature

Figs. 4–6 show the results of measured temperature distributions. Three different heating powers are tested, and different levels of liquid coverage examined. In addition, three spacings between the cylinders are tested. All the results show a clear increase in liquid temperature in the liquid meniscus near the heated contact line. The trend in the temperature then shows a dip before continuing to increase to the temperature of the exposed cylinder. This temperature drop is believed to correspond to the evaporative thin film that cannot be detected from the optical image but can be determined reasonably well from the infrared image. By comparing the infrared image with the optical image, the apparent, bulk contact line detected by the optical image is located at the position where the temperature starts to decrease, reflecting the evaporation effect that justifies the high heat transfer rate in the thin film region. This observation encourages us to proceed to determine the thin film region dimension. To further establish confidence, we verify the accuracy of the results by changing the aiming angle of the camera to rule out the possibility of error due to radiation deflection. The results are found consistent.

From the results shown in Figs. 4–6 we see the liquid surface temperature before attaching the cylinder can be reasonably approximated by a piecewise linear

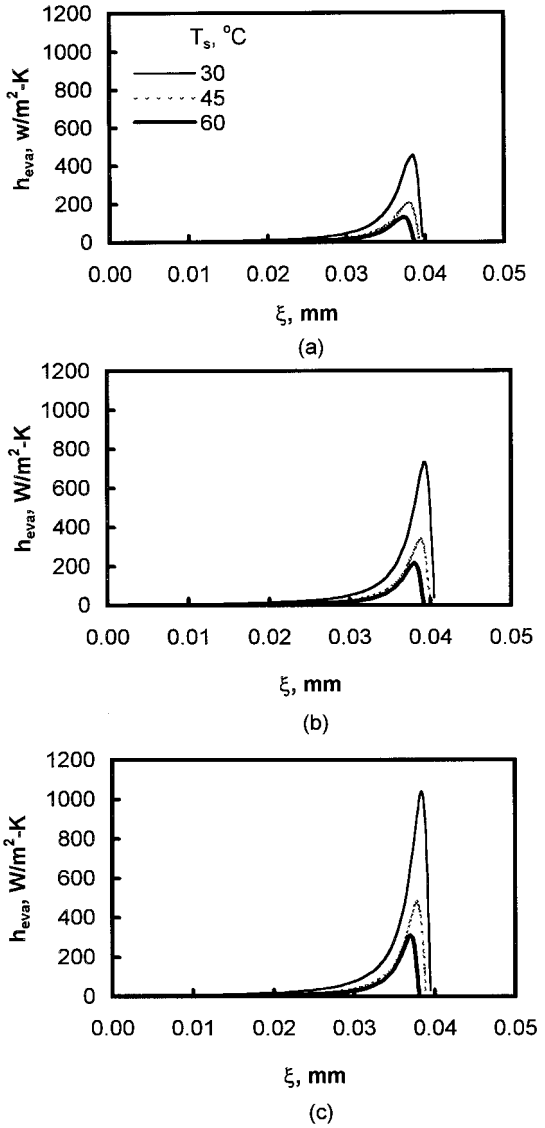

Fig. 13. Predicted thin film evaporative heat transfer coefficient: (a) $R_{sph}=2.25$ mm; (b) 3 mm; and (c) 3.75 mm.

relation that can be used as a boundary condition in the conjugate model to solve for local heat transfer rates. The following notable characteristics are clearly observed:

1. The increase in the spacing between two heated cylinders results in the increase in the center temperature only. The profile of temperature distribution near heated cylinders is almost the same.
2. The difference between solid surface temperature and center temperature strongly depends on the exposed solid surface temperature, T_s.
3. The liquid temperature near the heated cylinder increases linearly, and the slope of the linear part is dependent on the contacting location. Based on these observations, the following correlations are developed, using the definitions shown in Fig. 7(a):

Maximum temperature difference between solid surface and meniscus center:

$$\frac{\Delta T}{T_s}=1.058T_s^{0.851}. \tag{22}$$

The slope of the linear portion of liquid surface temperature:

$$\frac{\Delta T}{\Delta X}=\begin{cases}1.1666\,e^{2.3515(X/R_{sph})} & (X\geq 1/2R_{cyl})\\ 1.1666\,e^{1.1758(R_{cyl}/R_{sph})} & (X<1/2R_{cyl})\end{cases}. \tag{23}$$

Temperature drop in the evaporative thin film:

$$\delta T=\frac{T_s}{150}+0.3. \tag{24}$$

Comparison of Eqs. (22) and (23) with the experimental results from Figs. 4–6 are shown in Fig. 7(b) and (c). A good representation has been achieved (also see Figs. 4–6).

4.3. Thin film length

Fig. 8 presents the measured and predicted evaporating thin film length, l_d, from the Figs. 4–6 for different heating power and spacing between the cylinders. The three points in each line are for $R_{sph}=2.25$, 3.0 and 3.75 mm, respectively. The Bond number, *Bo*, is varied corresponding to three different quasi-steady temperatures; i.e., the surface tension is corrected according to the temperature value. In general, for the same diameter of the cylinder and spacing, the Bond number does not show significant effect on l_d. The increase in R_{sph}/R_{cyl} results in a decrease in l_d for a given Bond number. A comparison with the measured l_d indicates that the measured value is about an order of magnitude higher than the prediction. There are several reasons for this discrepancy. First, by carefully examining the experimental results as shown in Fig. 4, there are evidences that the temperature dips may occur within the length much smaller than that modeled by Fig. 7(a). Secondly, the surface is inevitably contaminated somehow by impurities during experimental processes. This change in the thin film geometry as caused by contamination cannot be detected by the current experimental method. The assumption in the thin film model of neglecting the effect of curvature [Eqs. (14) and (19)] may also contribute to the discrepancy between the measured and predicted l_d. It should be mentioned that the thin film model requires the specified l_s (see Fig. 1), a characteristic length from the static meniscus profile. The selection of l_s is somewhat

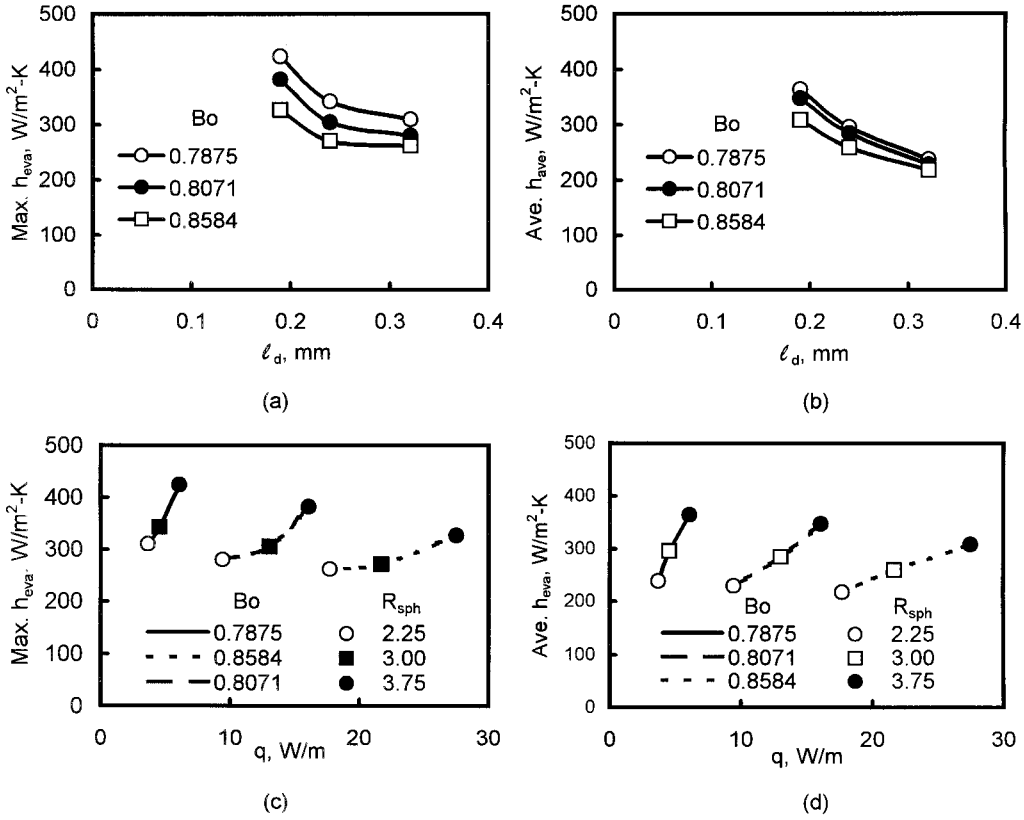

Fig. 14. Effects of heat generation and thin film length on the maximum and average heat transfer coefficient.

arbitrary. It is, however, bounded by the physical constraint that if l_s is too large, the value for the initial thickness of thin film is too high, violating the one-dimensional micro-flow characteristics in the thin film region. We conducted a parametric study and concluded that the selected l_s gives the best, physically meaningful results as judged by the local heat transfer characteristics results presented below. In this study, we may simply refer the thin film length determined by experimental approach as the macroscopic thin film length, and the one based on the modified Young–Laplace model as the microscopic thin film length.

4.4. Evaporative heat transfer coefficients

From the finite element model, local heat transfer coefficients from the liquid surface and exposed solid surface are determined from the normal temperature gradient as

$$h = -\frac{k_l}{\Delta T}\frac{\partial T}{\partial n}, \tag{25}$$

where ΔT is the temperature difference between the surface temperature and ambient gas temperature. A 20°C ambient temperature is chosen. The results are shown in Figs. 9–11. It should be remembered that the results are obtained from the combined experimental and finite element numerical analysis. For all the cases, the maximum values of h are corresponding to the evaporating thin film region and therefore, are named evaporative heat transfer coefficients. The evaporative heat transfer coefficient is 2.5 to 3 times higher than that from the rest of solid and liquid surfaces. The values in the center region of the liquid show a second maximum value for small spacing between glass cylinders, e.g., $R_{sph} = 2.25$ mm. As R_{sph} increases, the trend in h is reversed. This can be explained from the liquid velocity profile from numerical simulation. As seen from Fig. 12, there exists a vortex near the contact region in the liquid for each cylinder. For otherwise the same conditions, the closer spacing between two cylinders means two vortexes get closer; therefore, the convection near the central region is enhanced compared to the case of higher R_{sph} values.

The distribution of evaporative heat transfer coefficient, h_{eva} predicted from Eq. (20), i.e., the thin film model, is shown in Fig. 13. It can be seen that an increase in solid surface temperature leads to a decrease in h_{eva} and slight shift of the maximum h_{eva}

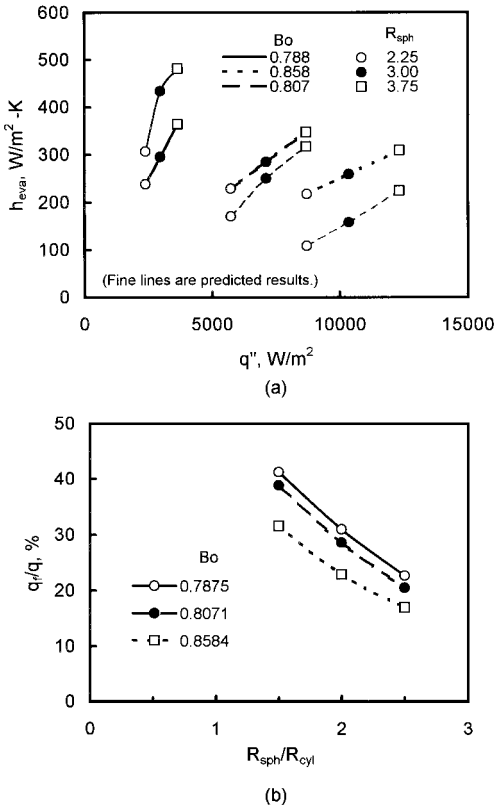

Fig. 15. (a) Comparison between the experimentally determined and predicted average heat transfer coefficient. (b) Ratio of evaporative heat transfer rate to the total heat generation.

towards a lower value of ξ, i.e., moving towards the bulk meniscus portion of the liquid. This is because the surface tension of ethanol decreases as temperature increases, and therefore, reduce the potential for sustaining the microscopic thin liquid film.

Similar trends can be found in Fig. 14 where the maximum and average heat transfer coefficients against the macroscopic thin film length are shown. Since the same fluid is used, the Bond number, Bo, represents the solid surface temperature. The high Bond number means a high surface temperature, i.e., the low surface tension. Again, the increase in the Bond number causes the decrease in h_{eva}. Although it is not as obvious for the microscopic thin film length in Fig. 13, the increase in the macroscopic thin film length in Fig. 14 shows a decrease in h_{eva}. In Figs. 14(c) and (d), it can be seen that the average evaporative heat transfer coefficient increases almost linearly with the input power for a given Bond number, while the maximum local evaporative heat transfer coefficient exhibits a non-linear fashion. For a fixed spacing between cylinders, h_{eva} decreases as the heating power increases.

Fig. 15(a) summarizes the effect of the surface heat flux and spacing between cylinders on the average heat transfer coefficient. Both experimental and prediction results show similar trends. For the same Bond number, an increase in R_{sph} results in an increase in h_{eva}, and an increase in heat flux also leads to an increase in h_{eva}. If we keep the values determined by the semi-empirical approach as a base, the h_{eva} determined by the thin film model tends to be overpredicted with the low Bo and underpredicted with the high Bo. For $Bo = 0.807$, the discrepancy is within 18%.

4.5. Ratio of evaporative heat transfer to total heat transfer

To evaluate the significance of the evaporative heat transfer for a partially wetted surface, the ratio of evaporative heat transfer rate to the total heat rate supplied to the cylinder is calculated. The results are presented as a function of R_{sph}/R_{cyl} in Fig. 15(b), where the heat transfer rate from the evaporating thin film is defined as

$$q_f = q'' l_d = h(T_s - T_\infty) l_d \tag{26}$$

The percentage of the heat transfer in the thin film region depends on cylinder spacing and quasi-steady surface temperature. It can be seen that although the evaporating thin film region is very small (l_d is the order of 100 μm), it can transfer 20 to 40% of heat power. The following correlation is derived to express the percentage of evaporating heat transfer as a function of the Bond number and R_{sph}/R_{cyl}:

$$\frac{q_f}{q} = (17.545Bo^2 - 27.781 \; Bo + 10.639)\ln(R_{sph}/R_{cyl}) + 0.2676 \; Bo - 3.1517 \tag{27}$$

where q, W/m, is the input heating power per unit length of the cylinder.

5. Conclusions

In this study, evaporative thin film heat transfer characteristics is evaluated by three important variables: exposed solid temperature (reflected in the Bond number), heating power (or surface heat flux) and spacing between cylinders (characterized by R_{sph}/R_{cyl}). It should be mentioned that heat flux is not independent of temperature in this study. Based on the above discussion, the following conclusions can be drawn for a two-dimensional evaporative thin liquid film:

1. The characteristic length of an evaporating thin

film, which attaches to a heated cylinder, is independent of the Bond number and surface heat flux. It is strongly affected by the distance between adjacent cylinders and decreases as the distance increases. For ethanol–glass–air interface, the macroscopic evaporating thin film length is from 0.2 to 0.3 mm for the temperature range studied, and is one order of magnitude higher than the predicted value from the modified Young–Laplace model.

2. The average heat transfer coefficient of the evaporating thin film, h_{eva} depends on all three variables. It increases with the decrease in the Bond number and decreases with cylinder spacing (or with the increase in the evaporative thin film length). It is 2.5 to 3 times than that of liquid and solid surface.
3. A correlation to predict the evaporating thin film heat transfer has been developed.

Acknowledgements

The support from the Air Force Research Laboratory to Tennessee State University through the Contract No. F33615-96-C3201 is greatly appreciated. Dr Jiang is also grateful for the financial support from the NSF through the Grant No. HRD-9702-6268.

References

[1] S.G. Bankoff, Significant questions in thin liquid film heat transfer, Journal of Heat Transfer, ASME Trans. 116 (1994) 10–16.
[2] E.A. Saez, Hydrodynamics and lateral thermal dispersion for gas–liquid concurrent flow in packed beds. Ph.D. thesis, University of California-Davis, 1983.
[3] M. Kaviany, Principles of Convective Heat Transfer, Springer-Verlag, New York, 1994.
[4] A. Marmur, Contact angle and thin-film equilibrium, Journal of Colloid and Interface Science 148 (1992) 541–550.
[5] A. Mirzamoghadam, I. Catton, A physical model of the evaporating meniscus, Journal of Heat Transfer, ASME Trans. 110 (1988) 201–207.
[6] M.B. Williams, S.H. Davis, Nonlinear theory of film ruptures, Journal of Colloid Interface Science 90 (1982) 220–228.
[7] J.P. Burelbach, S.G. Bankoff, S.H. Davis, Steady thermocapillary flows of thin liquid layers; II. experiment, Physics of Fluids A 2 (1990) 22–33.
[8] S.W. Joo, S.H. Davis, S.G. Bankoff, Long-wave instabilities of heated falling films: two-dimensional theory of uniform layers, Journal of Fluid Mechanics, ASME Trans. 230 (1991) 117–146.
[9] S. DasGupta, I.Y. Kim, P.C. Wayner, Use of the Kelvin–Clapeyron equation to model an evaporating curved microfilm, Journal of Heat Transfer, ASME Trans. 116 (1995) 1007–1015.
[10] Y.-X. Tao, M. Kaviany, Simultaneous heat and mass transfer from a partially liquid covered, two-dimensional surface, Journal of Heat Transfer, ASME Trans. 113 (1991) 874–882.
[11] P.C. Wayner, A dimensionless number for the contact line evaporative heat sink, Journal of Heat Transfer, ASME Trans. 111 (1989) 813–814.
[12] Y.-X. Tao, Effect of surface saturation on evaporation rate. Ph.D. dissertation, University of Michigan, 1989.